AIAA SciTech Forum
8–12 January 2018, Kissimmee, Florida
2018 AIAA/AHS Adaptive Structures Conference

10.2514/6.2018-0798

Chord-Extension Morphing for Active Rotor Track and Balance

Jayanth Krishnamurthi* Farhan Gandhi†
Rensselaer Polytechnic Institute, Troy, NY, 12180

This study examines the effectiveness of an on-blade extendable tab mechanism for rotor track-and-balance. The tab is essentially a chord-extension morphing mechanism, implemented as an extendable trailing-edge-plate over a spanwise section of each blade. A simulation model of the UH-60 Black Hawk rotor with seeded imbalance is developed, with the extendable tabs minimizing the 1/rev (1P) vibratory loads using a weighted least-squares optimization method. The extendable tab has the ability to reduce the 1P in-plane forces over the entire airspeed range with very large reductions observed in hover. The tabs are unable to reduce 1P vertical forces in hover, but are very effective in reducing these vibratory loads in cruise. The extendable tab is moderately effective in reducing 1P in-plane moments over the range of airspeeds. Best reductions in 1P loads are achieved by employing an *active* tab mechanism (adjusted at different airspeeds) over a *passive* mechanism (with constant setting over the airpseed range), with the active tab yielding additional gains in 1P in-plane forces and moments in hover and in 1P vertical forces in cruise. In hover, an examination of the load reduction mechanism indicates that a seeded radial shear and root torsional moment imbalance is cancelled by the generation of net blade root chordwise shear and root flap bending moments, respectively, on orthogonal blades. In cruise, similar mechanisms were observed, but the generation of net radial shears and root torsional moments on parallel blades were also contributors to total reduction in 1P hub in-plane and pitching moment vibrations.

I. Nomenclature

c	=	nominal blade sectional chord (ft)
ε	=	tab extension length (% of nominal blade sectional chord)
η	=	tab deflection angle (deg)
C_l	=	sectional lift coefficient (normalized using extended airfoil chord)
C_d	=	sectional drag coefficient (normalized using extended airfoil chord)
C_m	=	sectional pitching moment coefficient (normalized using extended airfoil chord)
$C_{l_{eff}}$	=	sectional lift coefficient (normalized using nominal airfoil chord)
$C_{d_{eff}}$	=	sectional drag coefficient (normalized using nominal airfoil chord)
$C_{m_{eff}}$	=	sectional pitching moment coefficient (normalized using nominal airfoil chord)
α	=	sectional angle of attack (deg)
M	=	sectional mach number
ϕ	=	sectional elastic twist (deg)
$\vec{z}$	=	normalized 1/rev vibration vector
$\vec{u}$	=	tab control vector
F_x	=	hub longitudinal force (lbs)
F_y	=	hub lateral force (lbs)
F_z	=	hub vertical force (lbs)

*Graduate Research Assistant, Department of Mechanical, Aerospace, and Nuclear Engineering, AIAA Student Member
†Redfern Chaired Professor, Department of Mechanical, Aerospace, and Nuclear Engineering, AIAA Associate Fellow.

J = total cost function
L = hub roll moment (lbs)
M = hub pitch moment (lbs)
S_x = blade root radial shear (lbs)
S_y = blade root chordwise shear (lbs)
S_z = blade root vertical shear (lbs)
M_x = blade root torsional moment (ft-lbs)
M_y = blade root flap bending moment (ft-lbs)
T = vibration sensitivity matrix with respect control adjustments
V = Velocity (knots)
$()_k$ = pertaining to the k^{th} iteration
$()_z$ = pertaining to vibratory loads
$()_u$ = pertaining to control adjustments
$()_V$ = pertaining to each airspeed
$()_{0P}$ = pertaining to the steady component
$()_{1P}$ = pertaining to the 1/rev component
$()_{2P}$ = pertaining to the 2/rev component
$()_{base}$ = pertaining to the baseline case

II. Introduction

Blade-to-blade dissimilarities are prevalent in rotary-wing aircraft despite tight manufacturing tolerances. The unevenness between blades contributes to vibrations experienced in the fuselage, primarily at 1/rev (1P) but also at higher harmonics. Such a condition is commonly known as a rotor track-and-balance (RT&B) problem and can significantly increase crew and passenger fatigue, reduce component reliability, and shorten component life [1]. Historically, the solution to this problem involved passive adjustment of trim tabs on blades, pitch link lengths, and blade mass based on identified sensitivities to minimize vibration levels [2–4]. This process requires dedicated maintenance flights which are time-consuming, expensive, and necessitate adjustments to be made on ground. Since the adjustments also do not change with flight condition (e.g. cruise speed), the reductions in vibratory loads are sub-optimal across the flight envelope. The ability to change one or more of the adjustments in-flight allows for optimal settings at different flight conditions and can also compensate for progressive deterioration, which in turn would reduce the need for dedicated maintenance flights or eliminate them altogether. This approach falls under the umbrella of active track and balance.

Early efforts in this area focused on demonstrating feasibility of actuation mechanisms. Active trailing-edge tabs using shape-memory alloys (SMAs) [5–7] and electromechanical actuators [8] have been considered. However, only implementation aspects were evaluated and their effectiveness over passive trim tabs in reducing vibrations was not addressed. Recently, variable-length, low-bandwidth active pitch links were considered in Refs. 9–11 for in-flight tuning (IFT). In particular, Ref. 10 showed that the active pitch links *alone* were quite effective in minimizing vibration levels due to imbalance on a UH-60 rotor in the wind tunnel and were utilized successfully again on a CH-53G in flight tests [11].

Recently, the concept of rotor morphing has received significant attention in order to enhance performance of rotary-wing aircraft in diverse operating conditions. In particular, on-blade chord-extension morphing [12–16] has been found to be advantageous when the aircraft is operating in stall-dominant conditions. In Ref. 13, it was shown that for a UH-60A Black Hawk helicopter, chord-extension morphing could reduce rotor power requirements by as much as 18% and 4/rev vibratory hub loads by as much as 31% at high gross weight and altitude. The ability to selectively extend the rotor blade chord in stall-dominant conditions is advantageous over using fixed-geometry, wide-chord rotor blades as the latter results in undesirable profile drag penalties at moderate operating conditions (where the aircraft is not near the envelope boundary and susceptible to stall). Several chord extension mechanisms have been considered to demonstrate feasibility of the concept [14–16] and transient behavior and control of the aircraft undergoing chord-extension morphing was recently examined in Ref. 17.

Given the potential benefits and multi-functional nature of chord-extension morphing, the application of such a method for rotor track-and-balance presents a promising approach. The current paper evaluates

the effectiveness of this method on a simulation model of the UH-60 rotor with a seeded imbalance. As an alternative to the traditional *bendable* tab, chord-extension morphing is utilized as an *extendable* tab over a spanwise portion of the blade to minimize vibration due to blade dissimilarity. The resulting 1P vibratory loads are minimized using a weighted least-squares optimization method. The benefits of in-flight (active) tuning over conventional, on-ground (passive) adjustments to the tabs is assessed and sensitivity of the vibratory loads to tab adjustments over multiple flight regimes is also discussed in detail. Finally, the physics of the tab mechanism is examined to understand the source of vibration reduction over the flight regime.

III. Simulation Model

A simulation model of the UH-60 Black Hawk rotor has been developed in the Rotorcraft Comprehensive Analysis System (RCAS) [18]. Key properties of the rotor blade are described in Table 1.

Table 1 UH-60 Rotor Properties

Rotor Radius	26.8 ft
Blade Chord	1.73 ft (mean)
Blade Twist	Nonlinear
Rotor Speed	258 RPM
Shaft Tilt	Scheduled with airspeed
Solidity	0.0822
Hinge Offset	1.25 ft
Blade Airfoil	SC1095 (root to 40% span) SC1094R8 (40-83% span) SC1095 (83% span to tip)

A. Main Rotor

The structural model of the UH-60 rotor is composed of a series of elements including rigid bars, linear rotational and translational springs and dampers, a rigid body mass, hinges, sliders and 13 nonlinear beam finite elements [19]. The outboard tip of the blade is swept and the blade is twisted nonlinearly along the radius. The pitch control linkage is represented by a series of rigid bars and spring elements and the collective and cyclic pitch inputs are introduced through a slide element. The blade root hinge is offset slightly from the center of rotation and the actual elastomeric bearing on the hub is represented by three discrete coincident hinge elements for flap, lag, and pitch rotation of the blade. The blades themselves are modeled as elastic beams undergoing coupled flap bending, lag bending, and elastic torsion. To introduce aerodynamic forces, the blade planform is discretized into 27 aerodynamic segments. Elemental aerodynamic forces and moments per unit length are calculated using airfoil look-up tables and distributed (via interpolation) across the blade. The coupled aeroelastic response is calculated/applied in the locally deformed airfoil coordinates as the blade undergoes rigid and elastic deformations. Lastly, the rotor inflow is modeled using a 12 x 12 Peters-He finite-state dynamic inflow model [20]. Physical properties for all elements of the UH-60 rotor model were included as appropriate.

B. Active Extendable Tab

Instead of the traditional *bendable* trim tab, an alternative mechanism of an *extendable* trim tab is employed. This is accomplished through the use of an extendable trailing-edge plate (TEP) that has been used in prior studies as a method of chord-extension morphing [13]. The active, extendable tab mechanism is illustrated in Figure 1, taken from Ref. 13. As shown in the figure, the tab extension, ε, is given as a percent of the nominal airfoil chord and the angle of deflection, η, is measured relative to the baseline airfoil's chord line and is implemented between 63% and 83% of the blade span. The extension of the tab effectively alters

the sectional aerodynamic coefficients through the extended chord length as well as the change in resulting airfoil profile. These modified coefficients are calculated using computational fluid dynamics (CFD) analysis and are detailed in Ref. 21. The baseline model of the UH-60A rotor uses coefficients from airfoil tables for both SC-1095 and SC-1094R8 which are normalized with respect to the *nominal* chord whereas the coefficients reported in Ref. 21 are normalized with respect to the *extended* chord.

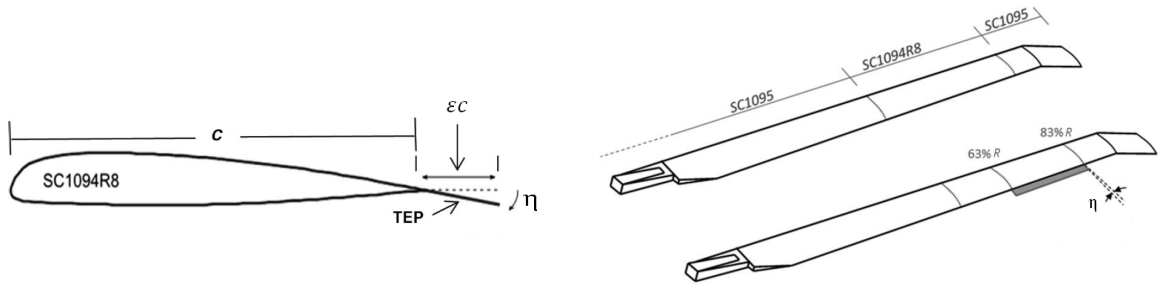

(a) TEP Extension - Airfoil (b) TEP Extension - Blade

Fig. 1 Chord Extension Mechanism, Ref. 13

To maintain consistency of implementation, the sectional aerodynamic coefficients (C_l,C_d,C_m) in Ref. 21 are re-normalized with respect to the *nominal* chord of the baseline airfoil. The relation between these normalizations is as follows:

$$\begin{aligned} C_{l_{eff}} &= (1+\varepsilon)\, C_l \\ C_{d_{eff}} &= (1+\varepsilon)\, C_d \\ C_{m_{eff}} &= (1+\varepsilon)^2\, C_m \end{aligned} \tag{1}$$

Doing so provides effective values for lift ($C_{l_{eff}}$), drag ($C_{d_{eff}}$), and pitching moment ($C_{m_{eff}}$) coefficients as a function of the *nominal* chord and also allows for ease of implementation in RCAS, where the tab is modeled as an aerodynamic flap segment. Lastly, the effective aerodynamic coefficients are tabulated into look-up tables as a function of angle of attack α, mach number M, and tab extension ε. Figure 2 shows these aerodynamic coefficients for the baseline SC-1094R8 airfoil and the modified variants that incorporate a maximum tab extension of $\varepsilon = 20\%$ and deflection angles of $\eta = 0°, 2°, 4°$, at a mach number of $M = 0.4$.

C. Imbalance Loads

Rotor smoothing on the UH-60 is typically conducted on the ground, in hover, and 80 knots, 120 knots, and 145 knots cruise [3, 4]. In Ref. 10, vibratory loads due to dissimilarity are reported for rotor advance ratios of $\mu = 0.2$ (90 knots) and $\mu = 0.35$ (155 knots) for the UH-60 rotor. To create a baseline vibration profile, these loads are then extrapolated to include hover, 80, 120, and 145 knots as well. For implementation in RCAS, mechanical point loads are applied with a specific magnitude and phase at the root of one blade such that appropriate vibration levels are generated at the hub for each airspeed.

D. Trim

A wind-tunnel trim procedure is carried out in RCAS for the UH-60A rotor. The rotor collective (θ_0), lateral (θ_{1c}), and longitudinal (θ_{1s}) cyclic pitch are used to trim the hub vertical force to 15,250 lbs and hub roll and pitch moments to 0 ft-lbs. The longitudinal shaft tilt angle (α_s is set at prescribed values scheduled with airspeed, shown in Table 2.

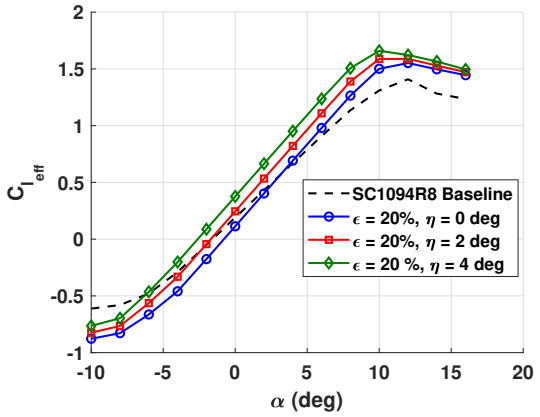

(a) Lift Coefficient

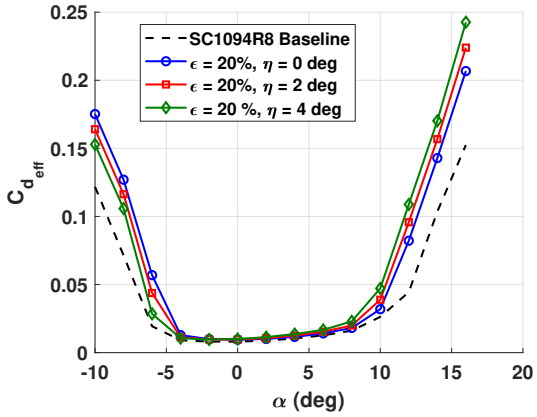

(b) Drag Coefficient

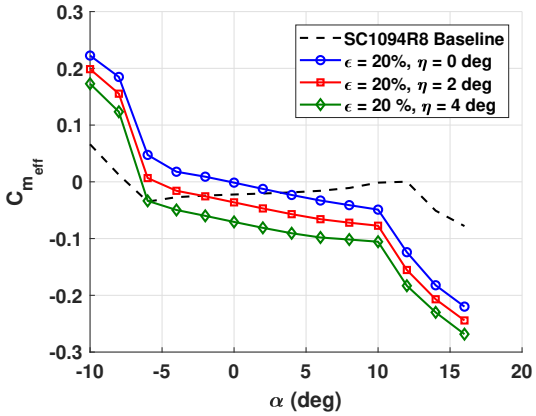

(c) Moment Coefficient

Fig. 2 Aerodynamic coefficients for baseline and extendable TEP for $M = 0.4$, normalized with respect to nominal chord, Ref. 21

Table 2 Rotor Longitudinal Shaft Tilt

V (knots)	α_s (deg)
0	0
80	−1.42
120	−4.5
145	−7

To trim the rotor at a given flight condition, an azimuthal step of 5° is used to calculate the aerodynamic loads on the blade and find a converged periodic solution for integrated rotor loads, inflow, and blade deformations over several revolutions. The three trim variables are then perturbed to determine the Jacobian matrix and trim steps are taken iteratively until the residuals of vertical force and roll/pitch moments are within specified tolerances.

IV. Minimization of Vibratory Loads

To minimize the vibratory loads resulting from rotor imbalance, a weighted least-squares optimization method is employed. Specifically, the 1/rev (1P) hub loads are targeted by the optimizer. The hub vibration levels can be written as a linearized equation in the following form:

$$\vec{z}_{k+1} = \vec{z}_k + T\Delta\vec{u}_k \tag{2}$$

$\vec{z}_k$ represents the vector of normalized 1P vibration magnitudes and $\vec{u}_k$ represents the vector of tab controls on each blade, respectively, for the k^{th} iteration in the optimization process:

$$\vec{z}_k = \begin{bmatrix} F_{x_{1P}}/F_{x_{1P_{base}}} \\ F_{y_{1P}}/F_{y_{1P_{base}}} \\ F_{z_{1P}}/F_{z_{1P_{base}}} \\ M_{x_{1P}}/M_{x_{1P_{base}}} \\ M_{y_{1P}}/M_{y_{1P_{base}}} \end{bmatrix}_k , \quad \vec{u}_k = \begin{bmatrix} \varepsilon_1 \\ \varepsilon_2 \\ \varepsilon_3 \\ \varepsilon_4 \end{bmatrix}_k \tag{3}$$

where $F_{x_{1P_{base}}}$, $F_{y_{1P_{base}}}$, $F_{z_{1P_{base}}}$, $M_{x_{1P_{base}}}$, and $M_{y_{1P_{base}}}$ are the baseline (uncontrolled) vibration levels. The variable T in Equation 2 is a sensitivity matrix, whose columns are obtained from the change in vector $\vec{z}_k$ by perturbing the elements of the vector $\vec{u}_k$, i.e. the Jacobian of the vibratory loads with respect to the controls. Both the calculation of 1P loads and the T-matrix are carried out in RCAS as part of the

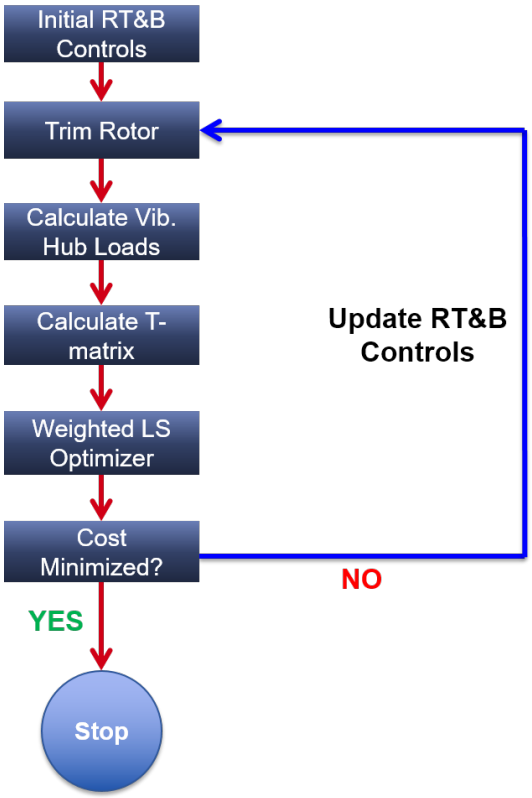

Fig. 3 Optimization Algorithm for Minimizing Vibratory Loads

optimization process. The scalar cost function for the optimization is written as

$$J = J_z + J_u = \vec{z}_{k+1}^{\,T} W_z \vec{z}_{k+1} + \vec{u}_k^{\,T} W_u \vec{u}_k \tag{4}$$

In Equation 3, J is a cost function that represents the sum of the weighted squares of the vibration measurements (J_z) and the control adjustments (J_u). W_z and W_u correspond to the weights pertaining to the

vibratory loads and control adjustments, respectively. In this study, both weighting matrices are set as identities

$$W_z = \mathcal{I}_{5x5} \ , \ W_u = \mathcal{I}_{4x4} \tag{5}$$

A schematic of the optimization process is shown in Figure 3.

A. Passive Track-and-Balance

For conventional passive track-and-balance procedures (with no in-flight adjustments), the $\vec{u}$ settings represent a compromise over the flight-speed regime. Thus, the optimization problem would be framed as

$$\begin{gathered} Determine \quad \vec{u} = \begin{bmatrix} \varepsilon_1 \\ \varepsilon_2 \\ \varepsilon_3 \\ \varepsilon_4 \end{bmatrix} \quad to \\ minimize \quad J_{comp} = J_z + J_u = W_{z_0} J_{z_0} + W_{z_{80}} J_{z_{80}} + W_{z_{120}} J_{z_{120}} + W_{z_{145}} J_{z_{145}} + W_u J_u \\ subject \quad to \quad 0\% \leq \vec{u} \leq 20\% \end{gathered} \tag{6}$$

The cost function pertaining to the vibration measurements (J_z) is now a sum of loads at multiple airspeeds. W_{z_0}, $W_{z_{80}}$, $W_{z_{120}}$, $W_{z_{145}}$ and J_{z_0}, $J_{z_{80}}$, $J_{z_{120}}$, $J_{z_{145}}$ correspond to the weights and cost functions pertaining to the vibratory loads, respectively, at those airspeeds. Note that a total of four tab settings are available in all, to minimize vibration levels over all flight speeds.

B. Active Track-and-Balance

Consider next, the case where the tab settings are active. The optimization problem is now solved separately at each airspeed, V, and framed as

$$\begin{gathered} Determine \quad \vec{u}_V = \begin{bmatrix} \varepsilon_1 \\ \varepsilon_2 \\ \varepsilon_3 \\ \varepsilon_4 \end{bmatrix}_V \quad to \\ minimize \quad J_V = J_{z_V} + J_{u_V} \\ subject \quad to \quad 0\% \leq \vec{u}_V \leq 20\% \end{gathered} \tag{7}$$

with J_{z_V} and J_{u_V} defined similar to Equation 4. The solutions would then take the form

$$\vec{u}_0 = \begin{bmatrix} \varepsilon_1 \\ \varepsilon_2 \\ \varepsilon_3 \\ \varepsilon_4 \end{bmatrix}_0 \quad \vec{u}_{80} = \begin{bmatrix} \varepsilon_1 \\ \varepsilon_2 \\ \varepsilon_3 \\ \varepsilon_4 \end{bmatrix}_{80} \quad \vec{u}_{120} = \begin{bmatrix} \varepsilon_1 \\ \varepsilon_2 \\ \varepsilon_3 \\ \varepsilon_4 \end{bmatrix}_{120} \quad \vec{u}_{145} = \begin{bmatrix} \varepsilon_1 \\ \varepsilon_2 \\ \varepsilon_3 \\ \varepsilon_4 \end{bmatrix}_{145} \tag{8}$$

Unlike the passive track-and-balance case, four tab settings are now available at *each* speed.

V. Results and Discussion

As mentioned earlier, representative 1P vibratory loads were seeded on the UH-60 rotor model and subsequently minimized over a range of airspeeds. For all results described in this paper, the tab is deployed at a deflection angle of $\eta = 2°$. Additionally, as part of the optimization procedure for both passive and active cases, multiple initial guesses for the control vector, $\vec{u}$, were tested in an effort to capture the best possible optimum at all airspeeds.

A. Minimization of 1P Loads

Figure 4 shows 1P hub lateral force, vertical force, and pitching moment loads. Both passive adjustments (that do not change over the airspeed regime), as well as active adjustments (determined at 0, 80, 120 and 145 knots) are considered. In hover, the passive tab shows a large reduction in 1P lateral force (Figure 4(a)), with the active tab showing further reduction (87% compared to 68%). At 80, 120 and 145 knots, both active and passive adjustments show comparable reductions in 1P lateral hub forces. Relative to hover, the reductions are seen to be modest at intermediate cruise speeds (80 and 120 knots), before increasing again somewhat in high-speed cruise (145 knots), but not to the levels of reduction observed in hover. 1P vertical force does not show any reduction in hover but progressively larger reductions are observed at increasing forward flight speeds (Figure 4(b)). Over the 80-145 knots flight speed range, active tab adjustments show significantly larger reductions in 1P vertical loads (87%) as compared to adjustments with the passive tab (46%). Modest reductions in 1P hub pitching moments (Figure 4(c)) are observed over the entire airspeed range with active tab adjustments showing only a small improvement (34%) in hover over the passive adjustments (24%). Figure 4(d) shows the required tab settings calculated from the optimization process. Clearly, the controls required to achieve the minimum vibration levels (particularly in vertical force) vary significantly with flight condition, which is only realizable with an active mechanism.

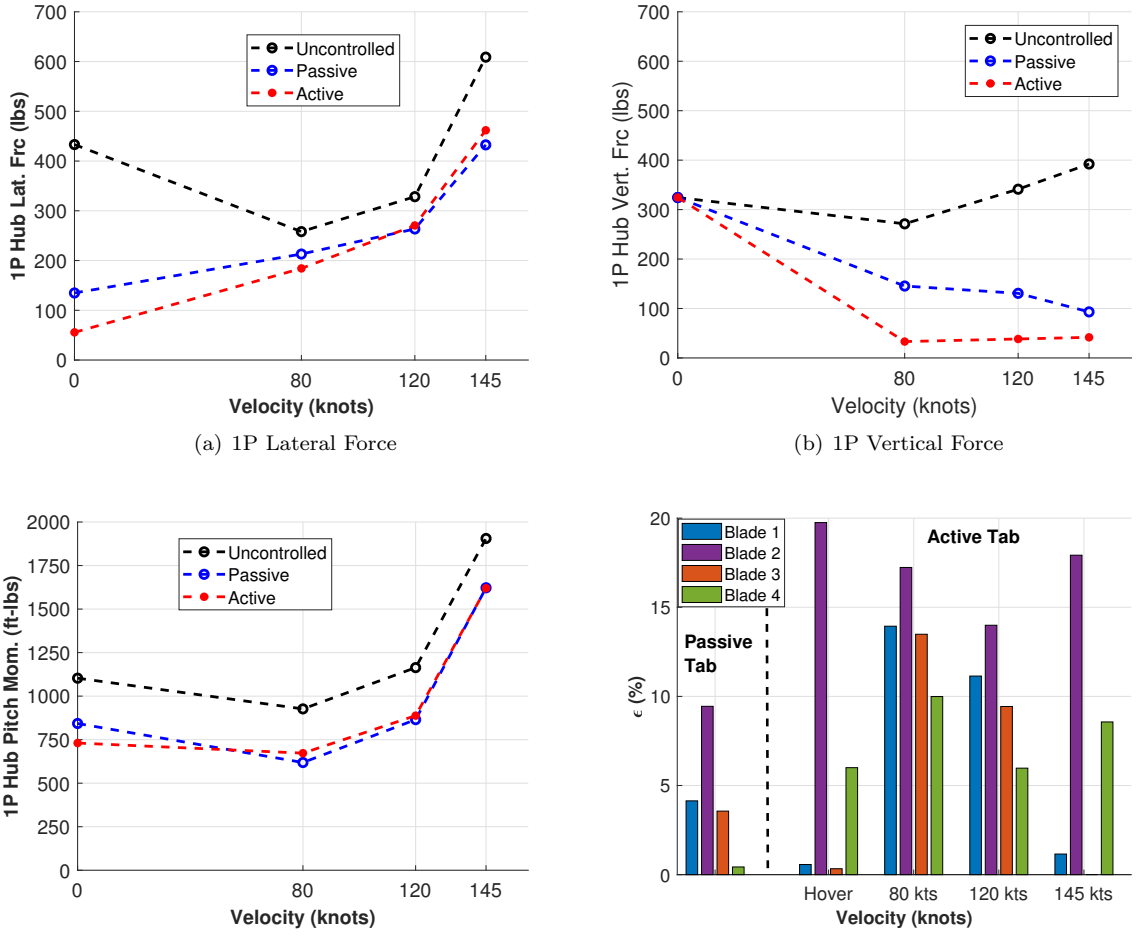

(a) 1P Lateral Force

(b) 1P Vertical Force

(c) 1P Pitching Moment

(d) Blade Tab Controls

Fig. 4 1P Vibration Levels and Tab Controls

B. Sensitivity Analysis

The sensitivity of the 1P loads to tab controls across flight speeds is shown in Figures 5-7. For each polar plot in these figures, the black dot indicates the magnitude and phase of the uncontrolled vibration levels. The tab on each blade is deployed *individually* from 0-20% and the corresponding change in 1P vibration level is indicated by the line associated with the specific blade. Figures 5(a)-5(d) show the sensitivity of the 1P lateral force to tab controls over the flight regime. The lateral force displays large sensitivity to tab deployment at hover. The sensitivity reduces significantly at 80 and 120 knots before increasing again at 145 knots (but not to the degree observed in hover). The trends shown Figures 5(a)-5(d) are consistent with the vibration results shown in Figure 4(a).

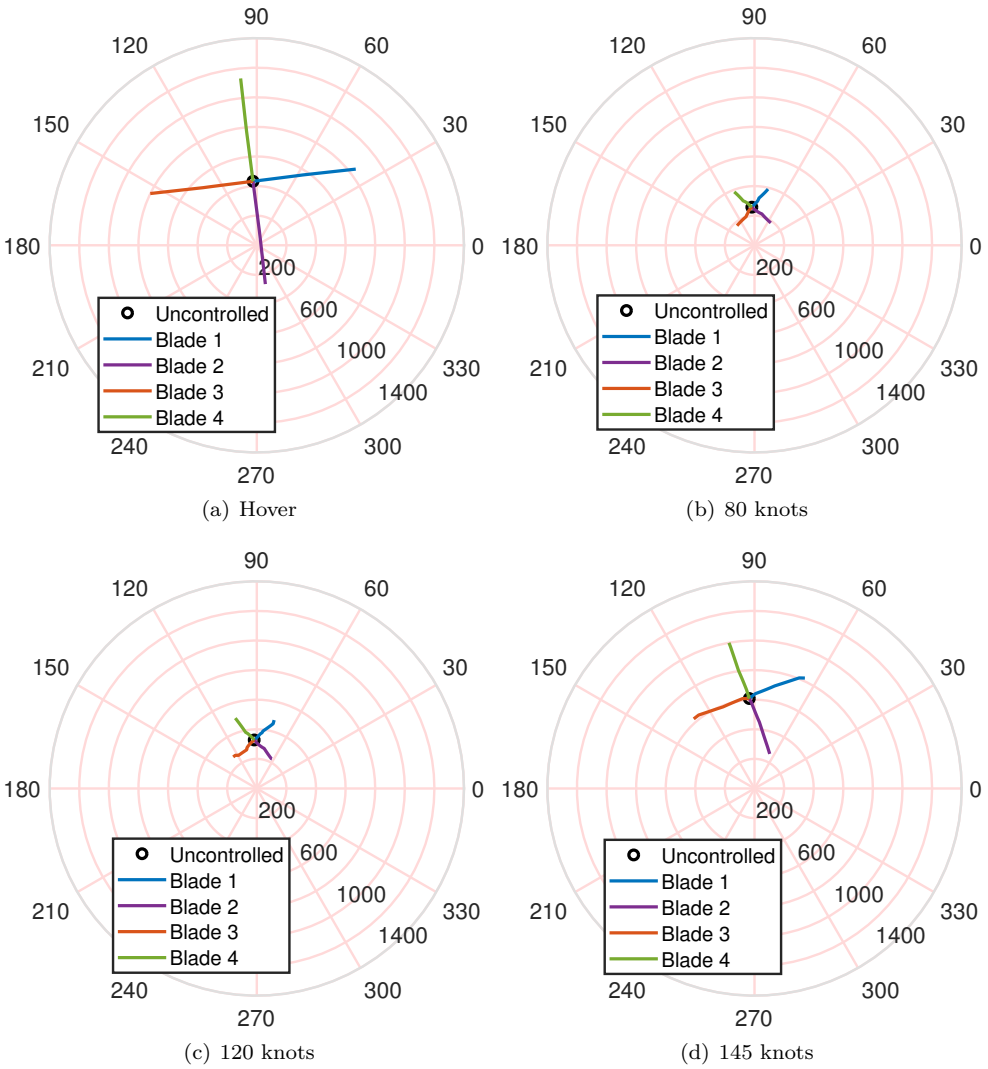

(a) Hover (b) 80 knots

(c) 120 knots (d) 145 knots

Fig. 5 1P Lateral Force Sensitivity to Tab Deployment

Figures 6(a)-6(d) show the sensitivity of the 1P vertical force to tab controls. Zero sensitivity is observed for vertical force in hover since quasi-static tab adjustments cannot generate any counteracting 1P vertical loads. In forward flight, however, the presence of cyclic pitch and azimuthal variation in incident velocity allow the generation of counteracting 1P vertical loads. From 80 to 145 knots, consistently high sensitivity is seen for 1P vertical force to tab deflection. The 1P pitching moment, over all airspeeds, shows moderate and generally similar sensitivity to changes in tab controls, as seen in Figure 7. As with the lateral force, the sensitivity trends of vertical force and pitching moment are consistent with the results shown in Figures 4(b) and 4(c), respectively.

It is interesting to note that the polar sensitivity plots all indicate that deployment of the tab on blade 2 would be most effective in reducing vibration. This is consistent with the optimized tab deflection results in Figure 4(d). In Figures 6(b)-6(d), the sensitivity of 1P vertical vibration levels in cruise to blade 2 tab deployment seems to be so strong that deploying this tab to its maximum (20%) could result in over-actuating the system. It is not surprising, then, that at 80 to 145 knots, the optimizer does not allow the tab on blade 2 to deflect to its maximum (Figure 4(d)) and appears to compensate, in part, with blade 4 tab deflection.

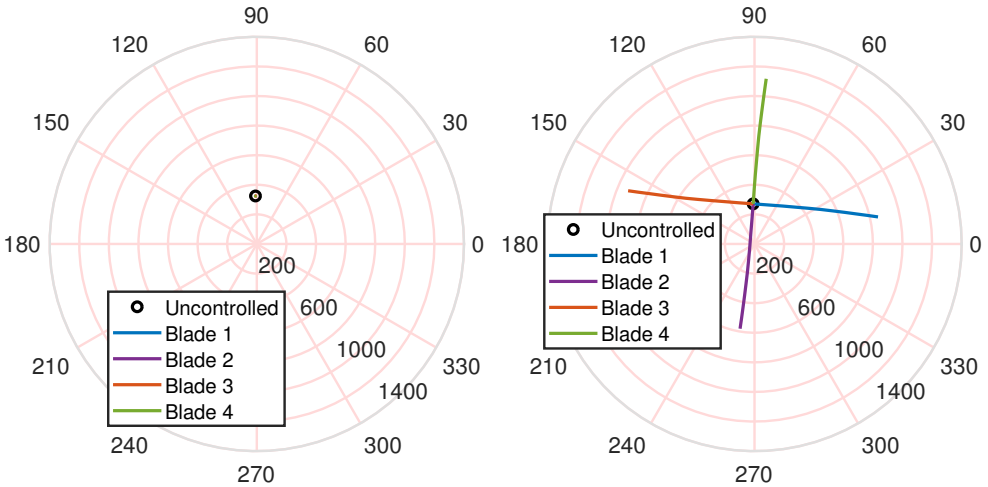

(a) Hover (b) 80 knots

(c) 120 knots (d) 145 knots

Fig. 6 1P Vertical Force Sensitivity to Tab Deployment

C. Physics of Extendable Tab

To understand the mechanism by which the vibratory loads are reduced, the underlying physics of the tab is now explored in further detail. With the focus specifically on the 1P vibratory loads at the hub, it is useful to consider the blade root shears and moments that are the contributing sources [22]. Table 3 summarizes the contributing components to the 1P loads at the hub, where S_x,S_y, and S_z are radial, chord-wise, and vertical blade root shears and M_x and M_y are blade root torsional and flap-bending moments, respectively. The coordinate system used for the root shears and moments is defined as follows: S_z is defined positive upwards, S_x is defined positive radially outward (towards blade tip), and S_y is defined positive in the direction of blade lead. For the moments, M_x is defined positive nose-up while M_y is positive for blade flapping downward.

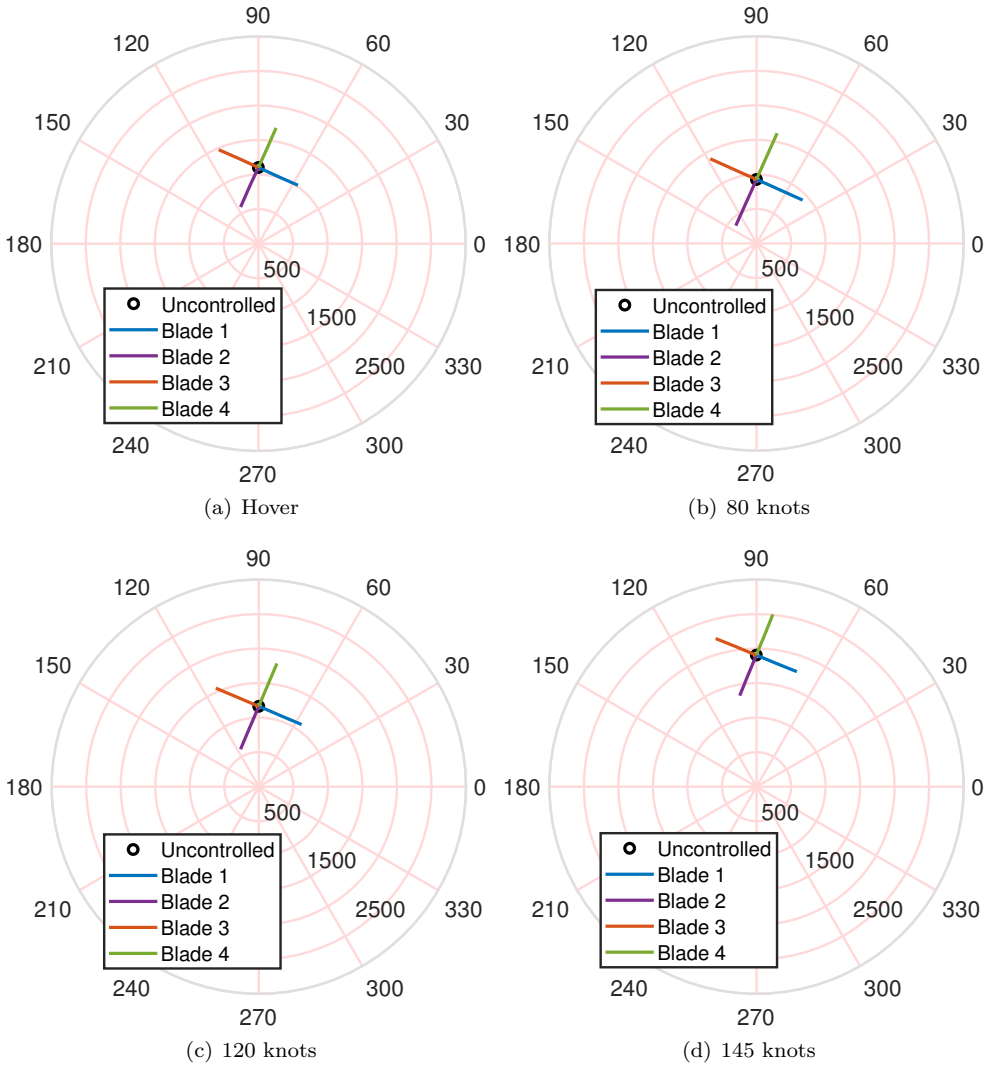

(a) Hover (b) 80 knots

(c) 120 knots (d) 145 knots

Fig. 7 1P Pitching Moment Sensitivity to Tab Deployment

Table 3 Transmission of Blade Root Shears to 1P Hub Loads

Hub 1P Loads		Blade Root Shears
$F_{z_{1p}}$	from	$S_{z_{1p}}$
$F_{x_{1p}}, F_{y_{1p}}$	from	$S_{x_{0p}}, S_{y_{0p}}, S_{x_{2p}}, S_{y_{2p}}$
L_{1p}, M_{1p}	from	$M_{x_{0p}}, M_{y_{0p}}, M_{x_{2p}}, M_{y_{2p}}$

1. Hover

The axisymmetric flow condition in hover facilitates ease of analysis and serves as a good starting point for understanding the operational mechanisms by which 1P vibration reduction is achieved. From Figures 2(a)-2(c), at $\eta = 2^o$, it is seen that the extension of the tab generally increases sectional lift, drag, and nose-down pitching moment. For the relatively torsionally compliant UH-60 rotor, a nose-down pitching moment induces a significant nose-down elastic twist. Figure 8(a) shows the change in twist on each blade corresponding to the active tab hover inputs from Figure 4(d). The large tab deflections on blades 2 and 4

are clearly observed to produce a nose-down elastic twist (relative to blades 1 and 3). Figure 8(b)) shows the corresponding change in chord-wise shear force on each blade. On both Figures 8(a) and 8(b), the dashed-dotted black vertical lines correspond to the 63% to 83% region over which the tab is present. While the drag on the blade 2 generally decreases along the span due to nose-down twist (resulting in a net positive ΔS_y), the local effect of the drag due to tab extension is clearly visible on Figure 8(b). In summary, a large chordwise force is generated on blade 2 (pointing toward the leading edge) and a smaller chordwise force is generated on blade 4 (also pointing to the leading edge) due to tab deflection on the two blades.

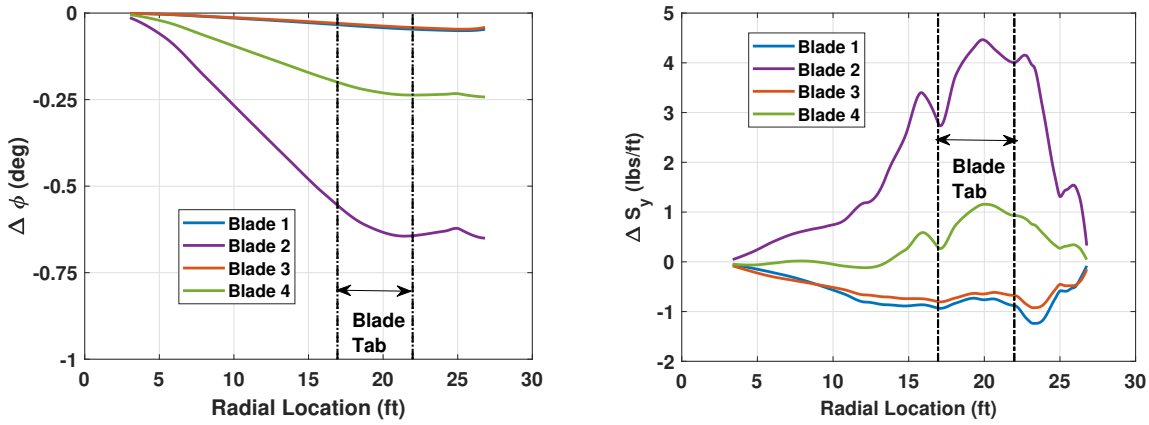

(a) Elastic Twist

(b) Chord-wise Shear

Fig. 8 Elastic Twist, and Chord-wise Shear in Hover

Figure 9(a) shows the magnitudes of seeded imbalance in radial shear ($\Delta S_{x_{0p}}$), vertical shear ($\Delta S_{z_{1p}}$), and torsional moment ($\Delta M_{x_{0p}}$) on blade 1 in the hover condition. Figures 9(b) and 9(c) pictorially depict the mechanism of vibration reduction through the extendable tab. The seeded imbalance in radial shear on blade 1 is counteracted by the change in steady chordwise shear ($\Delta S_{y_{0p}}$) generated on blades 2 and 4. Similarly, the seeded imbalance in torsion moment on blade 1 is counteracted by the change in steady flapwise bending moment ($\Delta M_{y_{0p}}$) on blades 2 and 4. The change in flapwise bending moment is primarily attributed to the change in lift on the blades due to the nose-down elastic twist seen in Figure 8(a).

2. 120 knots

Figure 10(a) shows the magnitude of seeded discrepancy in radial shear, vertical shear, and torsional moment on blade 1 at 120 knots. The mechanism by which 1P hub lateral and pitching moment vibrations are reduced remains broadly the same as in hover. However, at 120 knots, tab extensions are commanded on all four blades, as opposed to only blades 2 and 4 in hover (Figure 4(d)). In addition to change in chord-wise shear on blades 2 and 4, a changes in radial shear on blades and 1 and 3 also contribute to the reduction in total 1P lateral hub vibrations (Figure 10(b)). Similarly, in addition to change in flapwise bending moments on blades 2 and 4, a changes in torsional moments on blades and 1 and 3 also contribute to the reduction in total 1P hub pitching moment vibrations (Figure 10(c)).

VI. Conclusions

The current study focuses on the effectiveness of an extendable tab mechanism in reducing the 1/rev (1P) loads due to blade dissimilarity. The tab is essentially a chord-extension morphing mechanism, implemented as an extendable trailing-edge-plate over a spanwise section of each blade. A simulation model of the UH-60 rotor is developed in RCAS and imbalance loads are seeded on one blade to simulate dissimilarity. The resulting 1P vibratory loads are then minimized using a weighted least-squares optimization method. A comparative analysis of both active and passive tabs is considered. Sensitivities of the 1P vibratory loads to tab controls are examined across the range of airspeeds. Lastly, the physics of the tab mechanism is

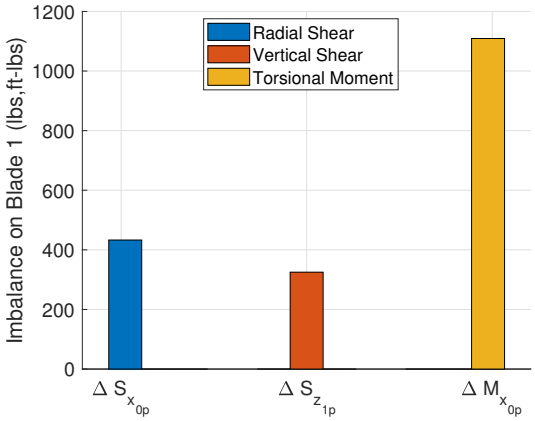

(a) Seeded Imbalance on Blade 1

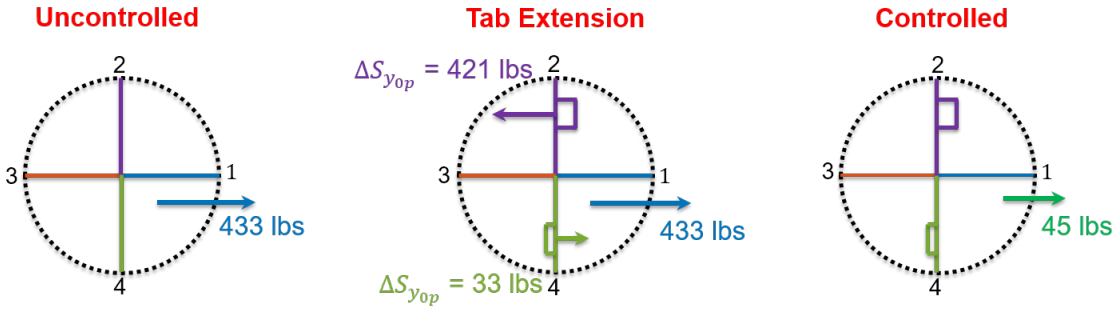

(b) Lateral Force

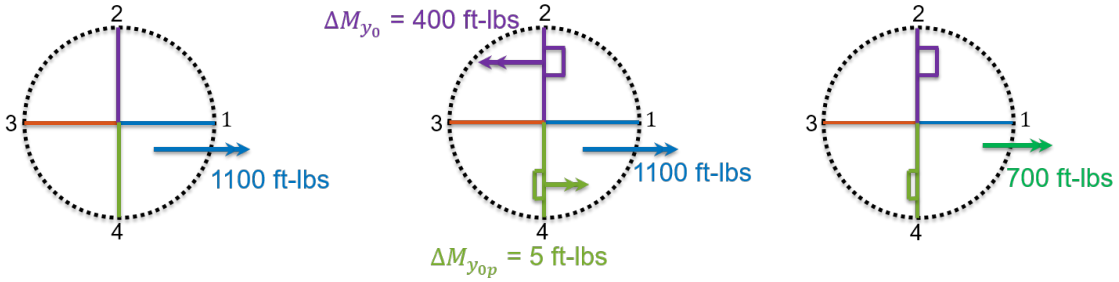

(c) Pitching Moment

Fig. 9 Tab Extension in Hover

explored in both hover and forward flight to understand the source of reduction in vibration. From the results presented in the paper, the following observations were drawn:

1) The extendable tab, as a mechanism has the ability to reduce 1P imbalance loads. Its greatest effectiveness is in reducing the 1P in-plane forces in hover, and the 1P vertical forces in cruise. In cruise, the 1P in-plane forces show moderate reductions, with these reductions increasing again, somewhat, at high speed. The extendable tab is unable to reduce the 1P vertical shear in hover but shows the ability to introduce moderate reductions in 1P in-plane moments over the entire range of airspeeds.
2) Using an active extendable tab, instead of a passive tab, results in additional reductions in 1P in-plane forces in hover (reductions of 87% compared to 68% with the passive tab). The active extendable tab also results in additional decrease in 1P vertical force in cruise. At 80 knots, the active tab generates reductions of 87% compared to reductions of 46% with the passive tab. For the 1P in-plane moments, the active tab shows slight improvement over the passive tab (reductions of 34% compared to 24%) in

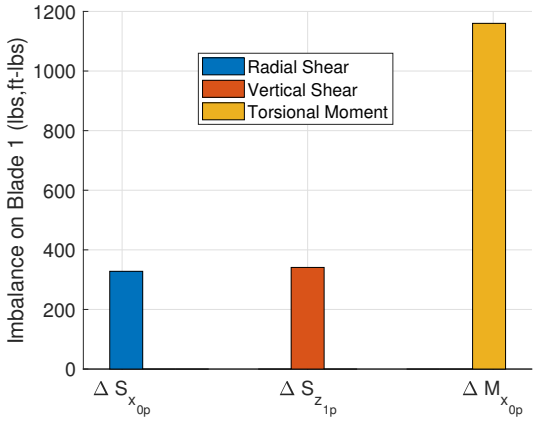

(a) Seeded Imbalance on Blade 1

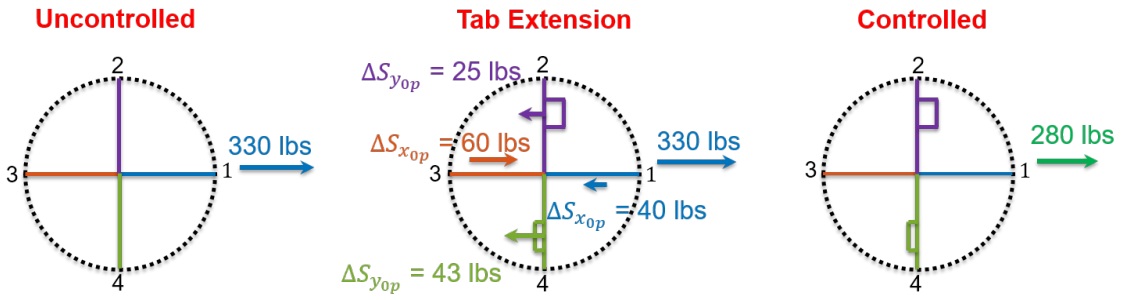

(b) Lateral Force

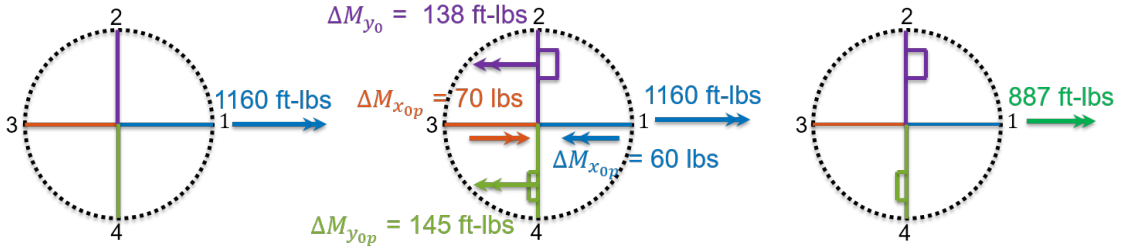

(c) Pitching Moment

Fig. 10 Tab Extension at 120 knots

hover. Best reductions in 1P vibration are achieved by varying the active tab inputs over the range of airspeeds. For seeded imbalance loads on blade 1, the optimizer yields active tab inputs for only blades 2 and 4 in hover and high-speed (145 knots), while tab extensions on all four blades are commanded at 80 and 120 knots. The passive tab extensions from the optimization results were observed to be lower than those of the active tab.

3) In hover, an examination of the imbalance load reduction mechanisms showed that generation of blade root chordwise shear on orthogonal blades (2 and 4 in the simulations carried out in this study) through the extension of the tab cancelled the seeded radial shear imbalance (on blade 1). Similarly, the generation of blade root flap bending moments on orthogonal blades (2 and 4) through tab extension negated the seeded blade root torsion moment imbalance (on blade 1). At 120 knots, similar mechanisms were observed, but changes in radial shear and torsion moment on blades 1 and 3 were also determined to be contributors to the total reductions in 1P hub lateral and pitching moment vibrations.

References

[1] Rosen, A., Ben-Ari, R., "Mathematical Modelling of a Helicopter Rotor Track and Balance: Theory," *Journal of Sound and Vibration*, Vol. 200, No. 5, 1997, pp. 589–603.

[2] Bechhoefer, E., Power, D., "IMD HUMS Rotor Track and Balance Techniques," *IEEE Aerospace Conference Proceedings, IEEEAC Paper No. 1191, Big Sky, Montana,*, 2003.

[3] Berry, J.D., Branhof, R.W., Keller, J.A., Lem Grant, CW5., Grabill, P., "Investigation of Automated Rotor Smoothing Using Continuous Vibration Measurements," *Proceedings of the American Helicopter Society* 60^{th} *Annual Forum, Baltimore, MD, June 7-10*, 2004.

[4] Branhof, R.W., Keller, J.A., Lem Grant, CW5., Grabill, P., "Application of Automated Rotor Smoothing Using Continuous Vibration Measurements," *Proceedings of the American Helicopter Society* 61^{st} *Annual Forum, Grapevine, TX, June 1-3*, 2005.

[5] Epps, J. J., and Chopra, I., "In-flight tracking of helicopter rotor blades using shape memory alloy actuators," *Smart Materials and Structures*, Vol. 10, No. 1, 2001, p. 104. URL `http://stacks.iop.org/0964-1726/10/i=1/a=310`.

[6] Kennedy, D.K., Straub, F.K., Schetky, L.McD., Chaudhry, Z., Roznoy, R., "Development of an SMA Actuator for In-Flight Rotor Blade Tracking," *Journal of Intelligent Material Systems and Structures*, Vol. 15, No. 4, 2004, pp. 235–248.

[7] Lengyel, A., van Schoor, M., Centolanza, L., Wilson, M., "Active Trim Tab for Rotor Track and Balance," *Proceedings of the AHS Aeromechanics Specialist's Conference, San Francisco, CA, Jan. 23-25*, 2008.

[8] Matalanis, C.G., Kuczek, A., Lin, R-S., Manes, E., Wake, B.E., Yeh, J., Chaudhry, Z., Brewer, P., "Development of an Active Trim Tab System for Onboard Rotor Tracking," *Proceedings of the* 66^{th} *AHS International Forum and Technology Display, Phoenix, AZ, May 11-13*, 2010.

[9] Norman T.R., Theodore, C., Shinoda, P., Fuerst, D., Arnold, U.T.P., Makinen, S., Lorber, P., O'Neill, J., "Full-Scale Wind Tunnel Test of a UH-60 Individual Blade Control System For Performance Improvement And Vibration, Loads, and Noise Control," *Proceedings of the American Helicopter Society* 65^{th} *Annual Forum, Grapevine, TX, May 27-29*, 2009.

[10] Fuerst, D., Arnold, U.T.P., Graham, D., "In-Flight Tuning: Wind Tunnel Test Results and Flight Test Preparation," *Proceedings of the* 67^{th} *AHS Annual Forum, Virginia Beach, VA, May 3-5*, 2011.

[11] Arnold, U.T.P., Fuerst, D., Hartmann, S., Hausberg, A., "Flight Testing of an In-Flight Tuning System on a CH-53G Helicopter," *Proceedings of the* 70^{th} *AHS Annual Forum, Montreal, Quebec, Canada, May 20-22*, 2014.

[12] Leon, O., Hayden, E., and Gandhi, F., "Rotorcraft Operating Envelope Expansion Using Extendable Chord Sections," *Proceedings of the* 65^{th} *AHS International Forum and Technology Display, Grapevine, TX, May 27-29*, 2009.

[13] Khoshlahjeh, M., and Gandhi, F., "Extendable Chord Rotors for Helicopter Envelope Expansion and Performance Improvement," *Journal of the American Helicopter Society*, Vol. 59, No. 1, 2014. doi:10.4050/JAHS.59.012007.

[14] Barbarino, S., Gandhi, F., and Webster, S., "Design of Extendable Chord Sections for Morphing Helicopter Rotor Blades," *Journal of Intelligent Material Systems and Structures*, Vol. 22, No. 9, 2011, pp. 891–905. doi:10.1177/1045389X11414077.

[15] Gandhi, F., and Hayden, E., "Design, Development, and Hover Testing of a Helicopter Rotor Blade Chord Extension Morphing System," *Smart Materials and Structures*, Vol. 24, No. 3, 2015. doi:10.1088/09645-1726/24/3/035024.

[16] Moser, P., Barbarino, S., and Gandhi, F., "Helicopter Rotor-Blade Chord Extension Morphing Using a Centrifugally Actuated Von Mises Truss," *Journal of Aircraft*, Vol. 5, No. 5, 2014, pp. 1422–1431. doi:10.2514/1.C032299.

[17] Krishnamurthi, J., and Gandhi, F., "Flight Simulation and Control of a Helicopter Undergoing Rotor Chord Extension Morphing," *Proceedings of the* 72^{nd} *AHS Annual Forum, West Palm Beach, FL, May 17-19*, 2016.

[18] Saberi, H., Khoshlahjeh, M., Ormiston, R., and Rutkowski, M., "Overview of RCAS and Application to Advanced Rotorcraft Problems," *AHS Fourth Decennial Specialists Conference on Aeromechanics, San Francisco, CA, January*, 2004.

[19] Hopkins, A.S., and Ormison, R.A., "An Examination of Selected Problems in Rotor Blade Structural Mechanics and Dynamics," *Proceedings of* 59^{th} *American Helicopter Society Annual Forum, Phoenix, AZ, May 6-8*, 2003.

[20] Peters, D.A., and He, C.J., "Correlation of Measured Induced Velocities with a Finite-State Wake Model," *Journal of the American Helicopter Society*, Vol. 36, No. 3, 1991, pp. 59–70.

[21] Bae, E.-S., and Gandhi, F., "CFD Analysis of High-Lift Devices on the SC-1094R8 Airfoil," *American Helicopter Society* 67^{th} *Annual Forum Proceedings, Virginia Beach, VA, May 3-5*, 2011.

[22] Johnson, W., *Rotorcraft Aeromechanics*, 1^{st} ed., Cambridge University Press, New York, NY, 2013.